



Effect of Turbulence Modeling on Overexpansion
and Flow Separation in RCS Thruster Nozzle
Extensions in Typical Crew Module
Configurations

Susheel Kumar Sekhar, Deepak Kumar Agarwal,
T. John Tharakan and S. Sunil Kumar

EasyChair preprints are intended for rapid
dissemination of research results and are
integrated with the rest of EasyChair.

October 26, 2023

Effect of turbulence modeling on overexpansion and flow separation in RCS thruster nozzle extensions in typical crew module configurations

Susheel Kumar S.* , Deepak Kumar Agarwal, T. John Tharakan and
S. Sunil Kumar

Liquid Propulsion Systems Centre, ISRO, Thiruvananthapuram 695547 India

[*susheelkumar_s@lpsc.gov.in](mailto:susheelkumar_s@lpsc.gov.in)

ABSTRACT

This paper investigates the aerodynamics of combusted plume gases in RCS thruster nozzles with extensions in a typical crew module firing at three identified altitudes (at $Z_a = 30\text{km}$, 14km and 7km) using CFD. Two thruster configurations of different nozzle extension lengths ($L_e = D_e$ and $3D_e$) are examined for flow separation and effective thrust, and inferences are drawn based on flow dynamics. Whereas nozzles with $L_e = D_e$ are able to generate over 95% of the expected thrust at 30 and 14km, for $L_e = 3D_e$, it drops to about 92% at 30km and 90% at 14km. At 7km, the thruster with $L_e = D_e$ shows a thrust reduction of around 12%, and it drops by a remarkable 45% for $L_e = 3D_e$. Such decrease is attributed to boundary layer separation within nozzle extensions due to overexpansion, which depends on the ratio of thruster combustion chamber pressure to ambient pressure, as well as scarfing of nozzle extensions. This paper documents the different flow features in RCS thruster nozzle extensions during their firing at different altitudes in a typical crew module configuration, and compares thrust estimates from using the RNG $k-\varepsilon$ and $k-\omega$ SST turbulence models.

Keywords: Nozzle overexpansion; Turbulence modeling of flow separation; Reaction Control System Thrusters

1 Introduction

Understanding the effect of ambient conditions on the flow inside nozzle thrusters and deducing the resultant thrust are key in determining Reaction Control System (RCS) thruster firing sequences for orientation maneuvers of crew modules during re-entry and flight abort, especially at lower altitudes. Reports on flow through convergent-divergent (CD) passages have been wide-ranging since the classical experiments of Carl G.P. de Laval, Aurel Boleslav Stodola and Ludwig Prandtl more than a century ago [1,2]. Typical pressure distribution curves with decreasing back pressures have since been documented in the divergent section of CD nozzles [1,3-5]. These well-regarded texts present the observations in simple axisymmetric nozzles assuming quasi-one-dimensional flow for a foundational understanding of the fluid mechanics. They describe the gradual transition from underexpansion to overexpansion as the back pressure decreases beyond the nozzle exit plane.

Numerous investigations, both experimental and numerical, have been conducted on overexpansion in launcher nozzles [6-9]. Understanding the dynamics of flow patterns such as the Mach disks and cap-like shock patterns near the nozzle exit plane is crucial in determining side-loads generated during launch. Distinct features such as free shock separation and restricted shock separation have been identified to optimize the contour designs of the divergent section. More recent numerical

studies have identified differences in predictions of such flow patterns and phenomena in this complex flow environment using various turbulence models [10,11].

For RCS thruster installations in crew modules, where space optimization is critical, nozzles are usually installed with tubular extensions that protrude from the ends of divergent sections. Whereas the flow remains largely attached in the divergent sections of these thrusters, contingent on the pressure ratio of the thruster combustion chamber pressure to the ambient pressure (P_c/P_a), significant separation can be expected in the extensions. The extent of separation here can have a substantial effect on the thrust generated by the nozzle, as well as impart side loads that have to be accounted for during orientation maneuvers. Unfortunately, there is a dearth in the literature on investigations into flow separation patterns in nozzle extensions for RCS thrusters. Furthermore, these extensions are often scarfed at the surface of spacecraft. Earlier studies on the effect of scarfing in nozzles were limited to estimates made using method of characteristics for axisymmetric flows [12,13]. More recent research on scarfing have been limited to performance analysis and optimization within a two-dimensional framework [14]. Only one documented report presents CFD simulation of RCS thruster firing in the Orion Crew Exploration Vehicle at different altitudes [15], briefly highlighting overexpansion of the thruster jet.

This effort investigates the effect of P_c/P_a on flow characteristics in nozzle extensions for RCS thrusters in a typical crew module for two different extension lengths, where the extensions are scarfed. Computational Fluid Dynamics (CFD) is used to simulate combusted gas flow through the nozzles, as well as beyond, at three identified altitudes in the Earth's atmosphere. The simulations are conducted in a stagnant ambient air in an effort to isolate effects of pressure gradient between the thruster chamber and the ambient at different altitudes. Indeed, during atmospheric re-entry, the presence of a bow shock ahead of the crew module could increase the local pressure present at the exit of the nozzle, further increasing the adverse pressure gradients in the nozzle extensions. Such an analysis is beyond the scope of the current paper, and the effect of the freestream is being investigated separately.

2 Computational Set-up

A typical crew module with pitch, yaw and roll thrusters is used in this study. The model is assumed to have twelve bi-propellant RCS thrusters distributed around its surface of which the pitch and yaw thrusters have $L_e = D_e$ and the roll thrusters have $L_e = 3D_e$, where D_e is the exit diameter of the nozzle and L_e is the length of the nozzle extension. Six of the twelve thrusters are assumed to be firing simultaneously representing a worst case abort condition. In the model, all surface features are retained for a realistic representation of the flow environment, including adjacent non-firing nozzles and surface cavities.

The overall computation domain and close-up views of slices of the computational domain are shown in Figures 1 and 2, respectively. The domain extends $6.67D$ along the radial direction to allow for the unimpeded expansion of plume gas, and $1.67D$ upstream and $2.33D$ downstream in the axial direction, where D is the largest diameter of the crew module. This domain is meshed using around 25 million hexahedral grid cells. Bodies of interest (BOIs) are set up in the nearfield of the module and the nozzle exits, with well refined grid cells resolving the plume flow within and outside of the thrusters. Grid cells of 1mm dimension are used within the nozzles with a $y^+ \approx 5$, the nearfield is meshed with 30mm grid cells, and the farfield with 250mm grid cells.

A commercial Navier-Stokes equations solver (ANSYS Fluent 2022 R1) is used to conduct thruster firing simulations from the nozzle inlet at three ambient conditions (Table 1). The conservation equations are solved using Fluent's density-based solver with an implicit time-stepping formulation for steady state, and AUSM+ scheme for the inviscid fluxes (2nd order accurate) and central differencing for the viscous terms. Gradients are estimated using node-based Green-Gauss formulation, and Venkatakrisnan limiter is used for spatial discretization.

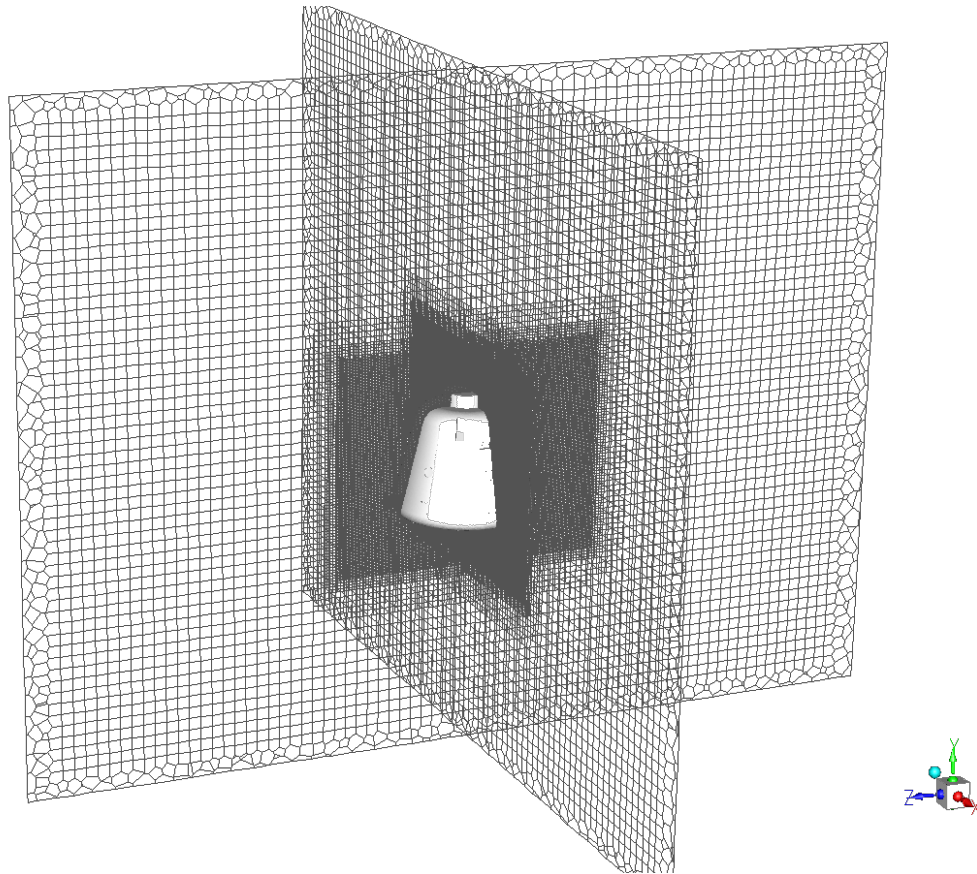


Figure 1 Computational domain showing BOIs in the nearfield of the CM, and coarser farfield grid cells

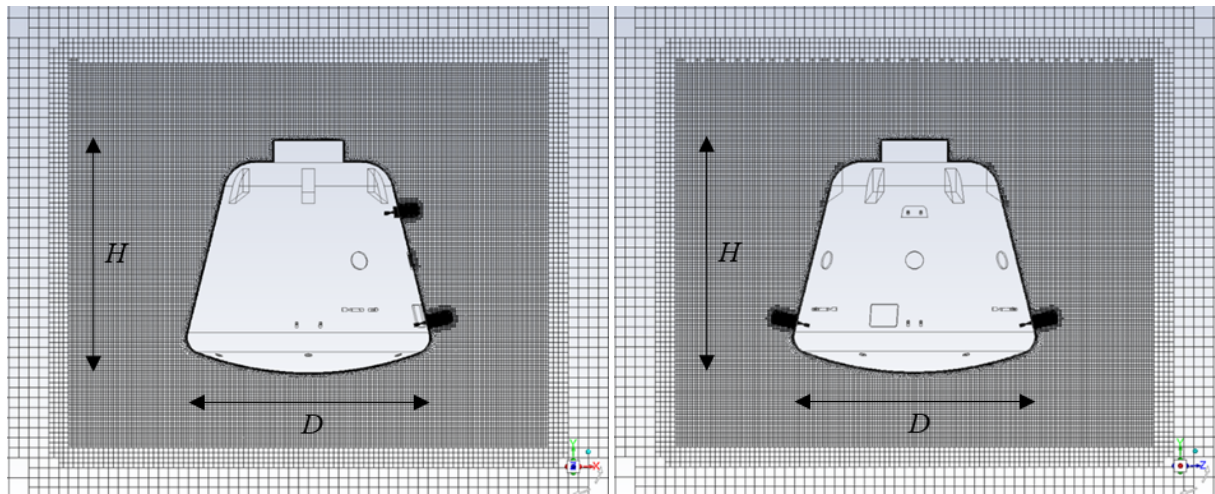


Figure 2 Mesh slices showing pitch (left) and yaw (right) planes, with refined near-field and thruster BOIs

For the boundary conditions (BCs), no-slip, cold wall BCs were set for all spacecraft surfaces except the nozzle surfaces that are fired. There, the walls set with an isothermal BC at 473K. For the farfield, pressure outlet BCs are set according to the ambient conditions at each altitude, with 5% turbulence intensity.

Combustion plume gas is considered a separate non-reacting species in the flow field, with monomethyl hydrazine (MMH) as the fuel and dinitrogen tetroxide (N_2O_4) as the oxidizer. Its properties are determined using NASA's Combustion Equilibrium Analysis code. Accordingly, the backwalls of the firing nozzles are set with appropriate pressures ($P_c = 7\text{bar}$) and temperatures ($T_c = 3031.6\text{K}$) for the pressure inflow BCs, to simulate combusted gas flow through the CD nozzles (with an area ratio of 10.5) estimated to generated around 100N of thrust.

Table 1 Ambient conditions

Z_a (km)	T_a (K)	P_a (Pa)	ρ_a (kg/m ³)	μ_a (kg/m ² s)	k_a (W/mK)	c_a (m/s)
30	226.509	1,197	0.01841	1.4753×10^{-5}	0.020361	301.71
14	216.65	14,170	0.22786	1.4216×10^{-5}	0.019533	295.07
7	242.7	41,105	0.59002	1.5613×10^{-5}	0.021703	312.31

In these 3D compressible flow simulations, turbulence is modelled using both the RNG k- ϵ model (with enhanced wall treatment), as well as the k- ω SST turbulence model. Both were used in their default implementation state, with production limiter and compressibility effects options activated.

3 Results and Discussion

Figures 3-6 show close-up views of combusted gas flow through the RCS thruster nozzle extensions and their expansion beyond, on vertical planes through the thruster axes, for $L_e = D_e$ and $L_e = 3D_e$. Instantaneous Mach number, temperature, density gradient and species mass fraction contours are shown from simulations using both the RNG k- ϵ and k- ω SST turbulence models.

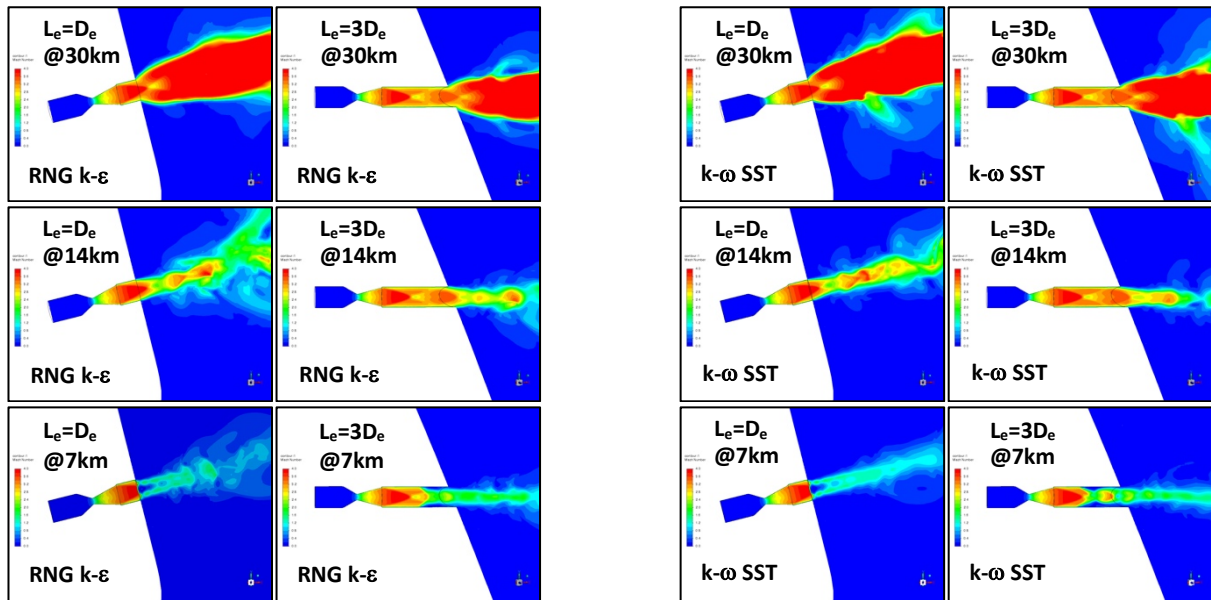


Figure 3 Instantaneous Mach number contours during firing of thrusters with $L_e = D_e$ and $L_e = 3D_e$, at 30km (top), 14km (middle) and 7km (bottom), using RNG k- ϵ (left) and k- ω SST (right) turbulence models

In Fig. 3, the top row shows the instantaneous Mach number contours of plume flow through the nozzles and extensions at 30km ($P_c/P_a = 585$), following by the same at 14km in the middle row ($P_c/P_a = 49$), and 7km in the bottom row ($P_c/P_a = 17$). The results from using the RNG k- ϵ turbulence model are shown on the left, and from using the k- ω SST turbulence model are shown on the right.

Evidently, at 30km (with $P_c/P_a = 585$), both turbulence models predict full flow through the nozzle and the extension for both $L_e = D_e$ and $L_e = 3D_e$. Flow acceleration through the divergent section of the nozzle and the oblique shocks emanating at the beginning of the nozzle extensions are clearly seen. For the longer extension, the shock diamond pattern with alternating oblique shock and Prandtl-Meyer expansion are also seen. Both turbulence models are seen to predict nearly identical flow patterns for both extension lengths, including the shape of the diverging shear layers from the exit of the extensions.

When the ambient pressure increases to $\approx 14\text{kPa}$ at 14km altitude (with $P_c/P_a = 49$), the flow patterns in the divergent section of the nozzles remain the same as at 30km , but differences start to become evident at the end of the extensions as well as the plume expansion beyond. The higher pressure ambient restricts the plume to a narrower profile, and the shear layers at the boundaries of the plume appear to be nearly parallel to the nozzle extensions. This results in the shock diamond pattern extending beyond the extensions due to reflections of the oblique shocks from the shear layers.

At 7km (with $P_c/P_a = 17$), the flow through the divergent section of the nozzles continue to be unperturbed, but the 41kPa ambient pressure alters both the flow in the nozzle extensions as well as the plume outside. For $L_e = D_e$, the presence of a Mach disk is clearly evident at the exit plane of the extension, which is a very short distance for the flow to adjust to the ambient pressure. This results in a strong normal shock, which also causes the boundary layer (BL) along the nozzle walls to start to separate. For $L_e = 3D_e$, the longer extension length allows for the effect of the higher ambient pressure to be felt upstream of the extension exit. Flow separation is observed at nearly 50% of the extension tube, and a shock train starts to appear immediately thereafter. It should be noted here that the scarfing of the nozzles starts to have an effect on the flow patterns too. Whereas scarfing is nearly perpendicular to the nozzle extension axis for $L_e = D_e$, for $L_e = 3D_e$, the nearly 70° scarfing angle results in an asymmetric flow pattern in the nozzle extension. The $k-\omega$ SST turbulence model seems to capture the asymmetry, along with the stronger oblique shock diamond, compared to RNG $k-\epsilon$.

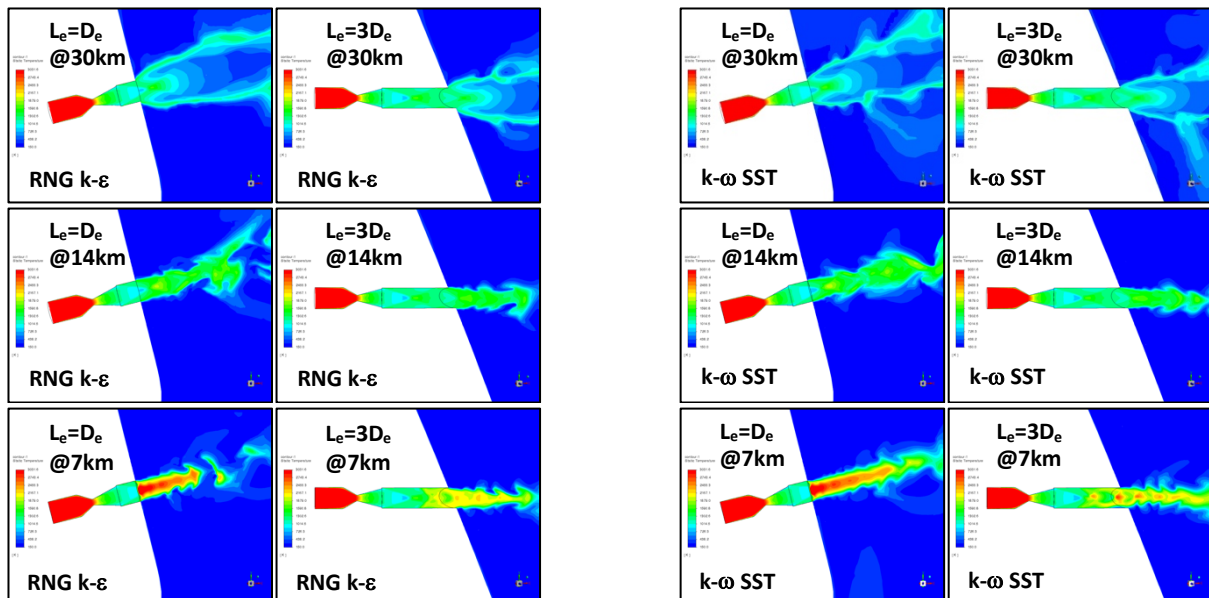


Figure 4 Instantaneous temperature contours during firing of thrusters with $L_e = D_e$ and $L_e = 3D_e$, at 30km (top), 14km (middle) and 7km (bottom), using RNG $k-\epsilon$ (left) and $k-\omega$ SST (right) turbulence models

Figure 4 shows the instantaneous temperature contours of plume flow through the nozzles and extensions at 30km ($P_c/P_a = 585$), following by the same at 14km in the middle row ($P_c/P_a = 49$), and 7km in the bottom row ($P_c/P_a = 17$). The variations in the temperature within the nozzle divergent sections and the extensions conform with the patterns noted with the Mach contours. The shear layers at the end of the extensions are clearly defined here at 30km , and the presence of shock diamonds at lower altitudes is evident with increased temperatures in the plume. At 7km , the high temperature behind the normal shock Mach disk is distinct, resulting in the plume temperature reaching nearly 3000K . The stronger shocks predicted by $k-\omega$ SST for $L_e = 3D_e$ at 7km is also evident here, with higher temperatures in the shock train, compared to RNG $k-\epsilon$.

Figure 5 shows the instantaneous density gradient contours of plume flow through the nozzles and extensions at 30km ($P_c/P_a = 585$), following by the same at 14km in the middle row ($P_c/P_a = 49$), and 7km in the bottom row ($P_c/P_a = 17$). These Schlieren-like plots are useful in highlighting sharp

gradients in the flow field, especially shock waves and shear layers. At 30km, for $L_e = D_e$, the oblique shock emanating from the start of the nozzle extension is clearly seen, as is the reflected shock pattern immediately outside of the extension. The shear layers spreading out from the lip of the nozzle extension are also seen here. For $L_e = 3D_e$, the reflected shockwave pattern within the nozzle extension is also clearly seen. At 14km, the flow field outside the extensions start to become busy, with additional shock reflections off the shear layers appearing downstream of the extension. Furthermore, two more weak oblique shocks appear at the end of the extension, where the shear layers start, and these overlap with the aforementioned shock diamond pattern. The asymmetry in these shock angles due to the scarfing of the nozzle extensions is also evident here. At 7km, these two shocks appear inside of the nozzle extensions for $L_e = 3D_e$, where the asymmetry is well captured by $k-\omega$ SST when compared with RNG $k-\epsilon$. For $L_e = D_e$, the presence of the strong normal shock at the exit plane is also clearly seen.

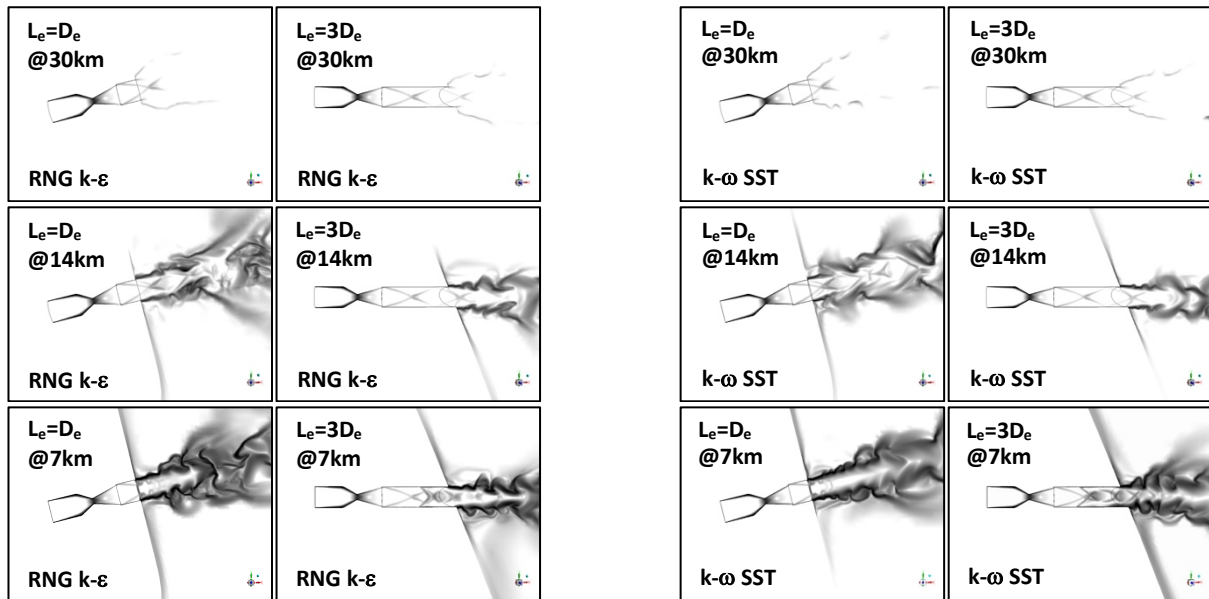


Figure 5 Instantaneous density gradient contours highlighting shockwaves and shear layers in thrusters with $L_e = D_e$ and $L_e = 3D_e$, at 30km (top), 14km (middle) and 7km (bottom), using RNG $k-\epsilon$ (left) and $k-\omega$ SST (right) turbulence models

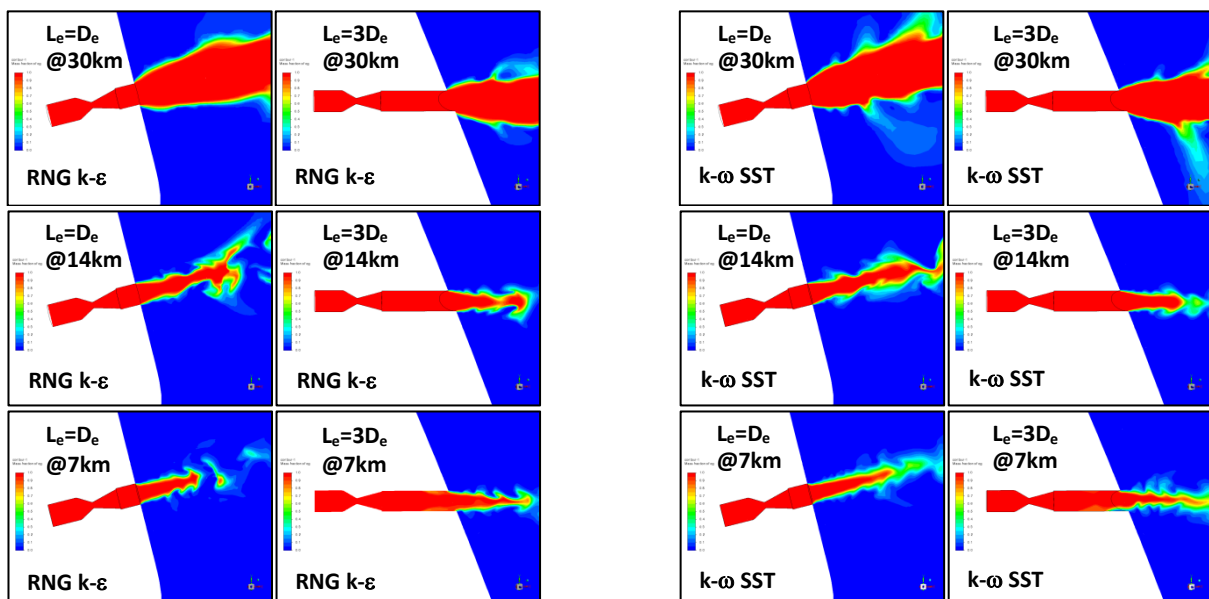


Figure 6 Instantaneous RCS thruster plume species mass fraction contours during firing of thrusters with $L_e = D_e$ and $L_e = 3D_e$, at 30km (top), 14km (middle) and 7km (bottom), using RNG $k-\epsilon$ (left) and $k-\omega$ SST (right) turbulence models

Figure 6 shows the instantaneous combusted plume gas species mass fraction plots for all the cases, which highlights the free expansion of the plume at higher altitudes, and the gradual confinement of the plume at lower altitudes, as well as the flow separation seen in the $L_e = 3D_e$ nozzle extensions at 7km.

Table 2 Thrust estimates at different altitudes using RNG k- ϵ and k- ω SST turbulence models

		k- ω SST	RNG k- ϵ	k- ω SST	RNG k- ϵ	k- ω SST	RNG k- ϵ
Z_a		30km		14km		7km	
P_a		1,197Pa		14,170Pa		41,105Pa	
$L_e = D_e$	v_e	2,473.38m/s	2,441.48m/s	2,432.03m/s	2,369.79m/s	2090.67m/s	1,938.0m/s
	T_{momentum}	97.29N	95.36N	96.25N	95.19N	85.93N	87.59N
	P_e	7,058.93Pa	7,204.05Pa	7,624.35Pa	7,978.11Pa	15,993.81Pa	17,407.5Pa
	T_{pressure}	6.65N	6.81N	-7.43N	-7.02N	-28.48N	-26.87N
$L_e = 3D_e$	v_e	2,421.59m/s	2,366.74m/s	2,336.34m/s	2,247.37m/s	1220.92m/s	1,187.64m/s
	T_{momentum}	95.12N	91.98N	92.91N	90.25N	57.42N	54.12N
	P_e	7,085.29Pa	7,352.1Pa	9,256.92Pa	9,752.51Pa	41,693.55Pa	39,720.21Pa
	T_{pressure}	6.68N	6.98N	-5.57N	-5.01N	0.67N	-1.57N

Table 2 presents the computed thrust values for the simulated RCS thruster firing at the three identified altitudes. In terms of the generated thrusts, at 30km altitude where $P_c/P_a = 585$, nozzles with $L_e = D_e$ were able to generate over 95% of the expected momentum thrust of 100N, and 92% with $L_e = 3D_e$. Similarly, at 14km ($P_c/P_a = 49$), a similar trend of generated thrust is evident (over 95% with $L_e = D_e$ and 90% with $L_e = 3D_e$). The differences between the theoretical and simulated values of thrusts are attributed to the scarfing of the nozzle extensions. At 7km ($P_c/P_a = 17$), the thruster with $L_e = D_e$ showed a thrust reduction of around 12%. This increased to a remarkable 45% for $L_e = 3D_e$, and is attributed to BL separation seen, due its interaction with shocks within the extensions creating a significant drop in the momentum thrust. Furthermore, the pressure thrust adds an additional 7N of thrust at 30km, reduces it by around 5N at 14km, and is nearly zero at 7km.

4 Conclusions

This paper compared the aerodynamics of combusted plume gases in RCS thruster nozzles with extensions in a typical crew module configuration, firing at three identified altitudes using RANS CFD. Two thruster configurations of different nozzle extension lengths were examined for flow separation and effective thrust, and inferences were drawn based on flow dynamics. Nozzles with $L_e = D_e$ were able to generate over 95% of the expected thrust at 30 and 14km, and a thrust reduction of around 12% was seen at 7km. For $L_e = 3D_e$, nearly 92% at 30km and 90% at 14km of the estimated thrust were achieved. At 7km, a remarkable drop of 45% was seen. Such decrease is attributed to boundary layer separation within nozzle extensions due to overexpansion, which depends on the ratio of thruster combustion chamber pressure to ambient pressure, as well as scarfing of nozzle extensions. These were presented in the form of contour plots of Mach number, temperature, density gradient and plume species mass fraction. The predictions were compared from using the RNG k- ϵ and k- ω SST turbulence models, and both models were shown to capture the major flow features well. The asymmetry in the shock pattern arising due to the scarfing of the nozzle is captured better using the SST turbulence model, compared to RNG k- ϵ .

References

- [1] Anderson, J.D. Jr., *Modern Compressible Flow: with historical perspective*, International ed., McGraw-Hill, Singapore, 1990.
- [2] Khare, S. and Saha, U.K., "Rocket Nozzles: 75 Years of Research and Development," *Sadhana*, Vol. 46, ID 76, 2021.
- [3] Liepmann, H.W. and Roshko, A., *Elements of Gas Dynamics*, Wiley, New York, 1957.
- [4] Shapiro, A.H., *The Dynamics And Thermodynamics Of Compressible Fluid Flow*, Ronald Press, New York, 1953.
- [5] John, J.E.A., *Gas Dynamics*, 2nd ed., Prentice-Hall, NJ, 1997.
- [6] Frey, M. and Hagemann, G., "Status of Flow Separation Prediction in Rocket Nozzles," Proceedings of the 34th AIAA/ASME/SAE/ASEE Joint Propulsion Conference & Exhibit, Cleveland, OH, July 1998. AIAA Paper 1998-3619.
- [7] Hagemann, G. *et al.*, "Advanced Rocket Nozzles," *Journal of Propulsion and Power*, Vol. 14, No. 5, pp. 620-634, 1998.
- [8] Terhardt, M. *et al.*, "Flow Separation and Side-load Behavior of Truncated Ideal Rocket Nozzles," Proceedings of the 37th AIAA/ASME/SAE/ASEE Joint Propulsion Conference & Exhibit, Salt Lake City, UT, July 2001. AIAA Paper 2001-3686.
- [9] Deck, S. *et al.*, "Numerical Simulations of Steady and Unsteady Separated Nozzle Flows," Proceedings of the 40th AIAA Aerospace Sciences Meeting & Exhibit, Reno, NV, January 2002. AIAA Paper 2002-0406.
- [10] Allamaprabhu, Y. *et al.*, "Numerical prediction of nozzle flow separation: Issue of turbulence modeling," *Aerospace Science and Technology*, Vol. 50, pp. 31-43, 2016.
- [11] Wang, L. *et al.*, "Comparative study on the performance of turbulence models in flow separation of large expansion ratio nozzle," *Journal of Physics: Conference Series*, 2364 012035, 2022.
- [12] Lilley, J.S. and Hoffman, J.D., "Performance Analysis of Scarfed Nozzles," *Journal of Spacecraft and Rockets*, Vol. 23, No. 1, pp. 55-62, 1986.
- [13] Lilley, J.S., "Design and Optimization of Propulsion Systems Employing Scarfed Nozzles," *Journal of Spacecraft and Rockets*, Vol. 23, No. 6, pp. 597-604, 1986.
- [14] Kogathi, H. and Nair, M.T., "Performance Analysis of Conical Scarfed Nozzles using CFD," Proceedings of the 21st AeSI Annual CFD Symposium, Bangalore, August 2019.
- [15] Zhang *et al.* "Research on RCS Jet Interaction Characteristics of the Capsule Entry Vehicle at Subsonic and Transonic Speed," *Journal of Physics: Conference Series* 2381 012111, 2022.
- [16] Stark, R.H., "Flow Separation in Rocket Nozzles, a Simple Criteria," Proceedings of the 41st AIAA/ASME/SAE/ASEE Joint Propulsion Conference & Exhibit, Tucson, AZ, July 2005.